Stacking model of a three-dimensional second-order topological insulator manifesting quantum anomalous Hall effect

B. Ostahie* and A. Aldea
National Institute of Materials Physics, POB MG-7, 77125 Bucharest-Magurele, Romania

(Received 29 November 2023; revised 11 March 2024; accepted 23 April 2024; published 14 May 2024)

We investigate the transport and energy spectrum properties of a three-dimensional high-order topological structure formed by stacking two-dimensional square diatomic Chern insulator lattices. Electron-hole symmetry and the energy spectrum degeneracy at individual points in the semimetallic phase are proven to be due to chiral and antiunitary symmetries in the periodic system. Additionally, we explore the influence of boundary conditions in a slab system with varying surface atom connectivity, and we demonstrate analytically the presence of zero-energy surface states in specific configurations. Moreover, we describe the emergence of two chiral hinge states driven by a perpendicular phase in the nanowire geometry. Next, the quantum Hall resistance is computed in the cross-configuration of a four-lead device. In this paper, we demonstrate that the trajectories of hinge states, determined by the number of layers in parallelepiped finite structure, give rise to fractional Hall plateaus.

DOI: 10.1103/PhysRevResearch.6.023168

I. INTRODUCTION

The investigation of topological properties in condensed matter began with studies of the quantum Hall effect (QHE), graphene, and other two-dimensional (2D) materials. In the next stage, the study of the three-dimensional (3D) systems revealed additional aspects, including higher-order topological phases characterized by specific topological modes. In general terms, the higher-order topological insulator (HOTI) of index N, defined in a D-dimensional space, would present topological states of the dimensionality $D - N$, where $N \geqslant 2$. For $N = 2$, the second-order topological insulator (SOTI) exhibits states along the hinges, and the third-order topological insulator (TI; $N = 3$) exhibits corner-type modes in 3D structures. The basic interest in these systems comes from the fact that the topological states are now the result of specific crystalline symmetries which, combined with the time-reversal (TR) symmetry, ensure their existence and robustness [1–3].

The different possible 3D trajectories of the chiral one-dimensional (1D) hinge states in the 3D structure may give rise to a quantum 3D Hall effect with different properties. Although the field is very recent, there are already several theoretical models and experiments that prove the existence of the higher-order topological states. Materials identified with such properties are, for instance, the chalcogenide crystals as Bi_2Se_3, a strong topological 3D insulator with a band gap of 0.3 eV [4]; Bi_1Te_1 and Bi_2TeI, dual 3D TIs exhibiting concurrent phases of both a weak TI and a topological crystalline insulator [5,6]; and Bi_4Br_4 in which the presence of topological hinge states was observed [7,8].

In addition to the real materials presented above, the HOTI phase can be experimentally proven in metamaterials like acoustic [9,10], phononic [11], or electrical circuit models [12,13].

The theoretical models for HOTIs have been developed by proposing Hamiltonians with chosen symmetries and checking for topological properties such as Dirac cones on some surfaces or hinge states at the joint of two surfaces. The TIs with an odd/even number of surface Dirac cones are classified as strong/weak TIs, respectively [14]. For crystalline insulators, Fu [15] introduced a TR tight-binding model with C_4 and C_6 symmetry, revealing the presence of gapless surface states on specific crystal facets. Schindler *et al.* [16] suggested a four-band Hamiltonian, again with C_4 symmetry, but with broken TR symmetry, which evidentiate chiral hinge states. The mirror symmetry is also sufficient for generating a SOTI, as shown by Ref. [1]. In the case of finite systems, the specific surface configurations (connectivity of the atoms at the surface) can affect the topological properties [17–19].

The aim of this paper is to advance a 3D SOTI model, with broken TR symmetry, which associates with the 3D quantum anomalous Hall effect (QAHE). The traditional QHE was observed in a 2D electron gas subject to a strong perpendicular magnetic field, resulting from the Landau levels structure. The discovery of the 3D QHE represented a significant breakthrough, and it was observed in 3D materials like Cd_3As_2 Weyl semimetal [20] and $ZrTe_5$ crystals [21]. The 3D QHE occurs in the presence of an external magnetic field, which affects Weyl orbits on opposite surfaces or creates one-sided hinge states in tilted magnetic field [22]. In contrast, in our approach, the breaking of TR symmetry is realized in the absence of an external magnetic field by the intrinsic Haldane-type phase.

*bogdan.ostahie@infim.ro

The transverse (Hall) current carried by chiral hinge states in a 3D structure is not a trivial problem [23,24]. Our analysis is done in steps, starting with the spectral properties of the fully periodical 3D structure, and going on with the slab and wire geometries, in the attempt to identify sufficient conditions for the emergence of the 3D QAHE. The Hall resistance is calculated in the Landauer-Büttiker formalism by attaching properly four leads in cross configuration.

The 3D model is obtained by stacking layers with Chern properties in a sequence with opposite chirality. The stacking method is widely used in theoretical models [25–27] because it allows for separate manipulation of intralayer and interlayer couplings. In our model, the main difference compared with other approaches consists of the phase attached to the interlayer hopping, which we called the vertical phase. This phase, together with a sufficiently strong interlayer coupling, gives rise to chiral hinge states that support QAHE. It turns out that this effect depends significantly on the number of layers (odd or even), as the hinge currents close differently in the two cases. Regarding the layers, the model consists of a 2D square lattice with two atoms per unit cell. The important parameters are the next-nearest-neighbor hopping and the internal phase of the Haldane type, which ensure the Chern insulator properties in each layer [28–30].

In Sec. II, we introduce the Hamiltonian model, analyze the energy spectrum of the periodic system, and explain the chiral and antiunitary symmetries, along with the behavior of the locus in the momentum space of the gap closing points in the semimetallic phase. Section III presents the slab and nanowire systems, wherein we analytically describe the properties of zero-energy surface states and the appearance of chiral hinge states in the wire geometry. Section IV covers the QHE and the spectrum properties of finite systems. The conclusions are summarized in the last section. In Appendix A, we explicitly show the Chern number as a function of the Haldane phase for one independent layer, and Appendix B provides detailed analytical calculations of the zero-energy localization properties.

II. HAMILTONIAN MODEL, SYMMETRIES, AND SPECTRAL PROPERTIES

We build up a tight-binding model for a 3D structure by stacking 2D diatomic lattices with opposing Chern numbers (see Fig. 1). In this case, the number of atoms in the unit cell is four: A (red), B (blue), C (green), and D (orange), and the primitive vectors are $\vec{a}_1, \vec{a}_2, \vec{a}_3$. In what follows, to introduce the Hamiltonian of our model, we define the creation $a^\dagger_{n,m,t}$, $b^\dagger_{n,m,t}$, $c^\dagger_{n,m,t}$, $d^\dagger_{n,m,t}$ and, respectively, annihilation $a_{n,m,t}$, $b_{n,m,t}$, $c_{n,m,t}$, $d_{n,m,t}$ operators corresponding to the atoms in the unit cell described by the lattice vector $\vec{R}_{n,m,t} = n\vec{a}_1 + m\vec{a}_2 + t\vec{a}_3$. The Hamiltonian can be divided into three terms. The first two terms H_1 and H_2 describe the layers which accommodate the atoms (A, B) and (C, D), while the third term $H_\perp$ represents the interlayer coupling:

$$
\begin{aligned}
H &= H_1 + H_2 + H_\perp;\\
H_1 &= \sum_{n,m,t} E^{\mathrm{A}} a^\dagger_{n,m,t} a_{n,m,t} + E^{\mathrm{B}} b^\dagger_{n,m,t} b_{n,m,t}\\
&\quad + t_1 \sum_{n,m,t} \exp(-i\gamma) b^\dagger_{n,m,t}(a_{n,m+1,t} + a_{n+1,m,t}) + \exp(i\gamma) b^\dagger_{n,m,t}(a_{n,m,t} + a_{n+1,m+1,t}) + \mathrm{H.c.}\\
&\quad - t_2 \sum_{n,m,t} a^\dagger_{n,m,t}(a_{n,m+1,t} - a_{n+1,m,t}) - b^\dagger_{n,m,t}(b_{n,m+1,t} - b_{n+1,m,t}) + \mathrm{H.c.},\\
H_2 &= \sum_{n,m,t} E^{\mathrm{C}} c^\dagger_{n,m,t} c_{n,m,t} + E^{\mathrm{D}} d^\dagger_{n,m,t} d_{n,m,t}\\
&\quad + t_1 \sum_{n,m,t} \exp(i\gamma) d^\dagger_{n,m,t}(c_{n,m+1,t} + c_{n+1,m,t}) + \exp(-i\gamma) d^\dagger_{n,m,t}(c_{n,m,t} + c_{n+1,m+1,t}) + \mathrm{H.c.}\\
&\quad - t_2 \sum_{n,m,t} c^\dagger_{n,m,t}(c_{n,m+1,t} - c_{n+1,m,t}) - d^\dagger_{n,m,t}(d_{n,m+1,t} - d_{n+1,m,t}) + \mathrm{H.c.},\\
H_\perp &= t_\perp \sum_{n,m,t} \exp(i\gamma_\perp) a^\dagger_{n,m,t} c_{n,m,t} + \exp(i\gamma_\perp) c^\dagger_{n,m,t} a_{n,m,t+1}\\
&\quad + t_\perp \sum_{n,m,t} \exp(-i\gamma_\perp) b^\dagger_{n,m,t} d_{n,m,t} + \exp(-i\gamma_\perp) d^\dagger_{n,m,t} b_{n,m,t+1} + \mathrm{H.c.}
\end{aligned}
\tag{1}
$$

In the above equation, E^{A}, E^{B}, E^{C}, and E^{D} are atomic site energies and will be taken as zero, t_1 and t_2 are the nearest-neighbor and next-nearest-neighbor hopping parameters in the O_{xy} plane, and $t_\perp$ is the hopping parameter that connects the consecutive 2D lattices in the O_z direction. The γ parameter in every 2D plane represents a periodic local magnetic flux which is chosen as in the Haldane model, the net total flux through any layer being zero (each layer is a Chern insulator, as we show in Appendix A). The $\gamma_\perp$ is a magnetic phase associated with the hopping parameter $t_\perp$. In this paper, we fixed the hopping parameter $t_1 = 1$ and the in-plane phase $\gamma = \pi/4$.

We start looking for the spectral properties of the Hamiltonian in Eq. (1) under periodic boundary conditions. To this aim, we need to use the Fourier transform of the creation and annihilation operators, as, for instance, $a_{nmt} = \sum_{\vec{k}} a_{\vec{k}} \exp(i\vec{k}\vec{R}_{nmt})$, where $\vec{k} = (k_x, k_y, k_z)$, and similarly for all the other operators. Then the Hamiltonian in Eq. (1) turns into a 4×4 matrix in the momentum space:

$$H = \sum_{\vec{k}} (a^\dagger_{\vec{k}}\ b^\dagger_{\vec{k}}\ c^\dagger_{\vec{k}}\ d^\dagger_{\vec{k}}) \mathcal{H}(\vec{k}) (a_{\vec{k}}\ b_{\vec{k}}\ c_{\vec{k}}\ d_{\vec{k}})^{\mathsf{T}},$$

$$\mathcal{H}(k_x, k_y, k_z) = \begin{bmatrix} -2t_2 f(k_x, k_y) & t_1 g(k_x, k_y, \gamma) & t_\perp h(k_z, \gamma_\perp) & 0 \\ t_1 g^*(k_x, k_y, \gamma) & 2t_2 f(k_x, k_y) & 0 & t_\perp h(k_z, -\gamma_\perp) \\ t_\perp h^*(k_z, \gamma_\perp) & 0 & -2t_2 f(k_x, k_y) & t_1 g(k_x, k_y, -\gamma) \\ 0 & t_\perp h^*(k_z, -\gamma_\perp) & t_1 g^*(k_x, k_y, -\gamma) & 2t_2 f(k_x, k_y) \end{bmatrix}, \tag{2}$$

where the notations $f(k_x, k_y)$, $g(k_x, k_y, \gamma)$, and $h(k_z, \gamma_\perp)$ are

$$\begin{aligned} f(k_x, k_y) &= \cos(k_x) - \cos(k_y), \\ g(k_x, k_y, \gamma) &= \exp(-i\gamma)\{1 + \exp[-i(k_x + k_y)]\} \\ &\quad + \exp(i\gamma)[\exp(-ik_x) + \exp(-ik_y)], \\ h(k_z, \gamma_\perp) &= \exp(i\gamma_\perp) + \exp(-i\gamma_\perp)\exp(-ik_z). \end{aligned} \tag{3}$$

The energy spectrum is derived through direct diagonalization of the Hamiltonian in the momentum representation. Analyzing the energy dispersion, in Fig. 2, we identify two distinct phases: semimetallic (for $t_2 = 0$ and any $\gamma_\perp$) and insulating (for $t_2 \neq 0$, also independently of $\gamma_\perp$). In Eq. (2), the Hamiltonian matrix contains the parameter t_2 placed on the diagonal, which controls the mass term. When t_2 is nonzero, the electrons acquire mass, resulting in the opening of a gap in the energy spectrum. This phenomenon is essential for understanding the transition between the semimetallic and insulating phases in the system. The expectation is that, under proper hard-wall boundary conditions, the insulating gap will be filled with hinge states, which will prove the topological character of this model Hamiltonian.

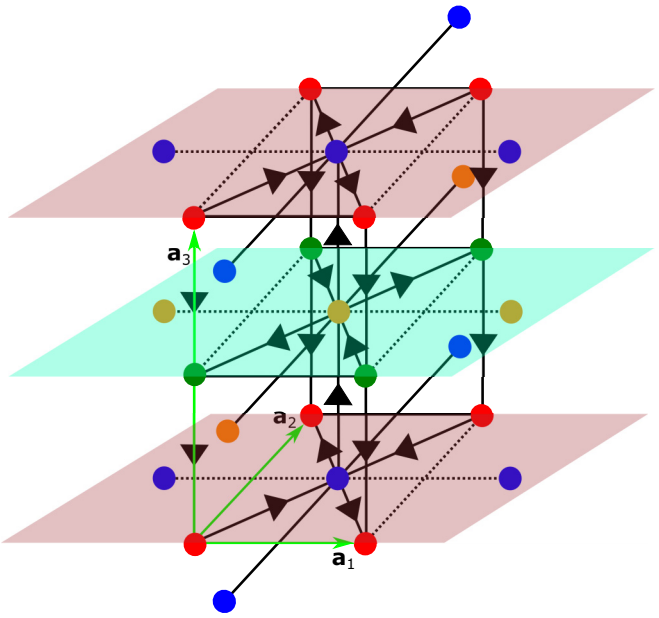

FIG. 1. Schematic representation of a cubic lattice obtained by stacking three layers. Note that the red and blue layers show opposite Haldane-type phases represented by in-plane arrows, and because of this, the unit cell contains four atoms, which are colored in red (atom A), blue (atom B), green (atom C), and orange (atom D). The in-plane arrows are associated with the hopping element t_1 and the vertical ones with $t_\perp$. The dashed and solid lines connecting atoms of the same kind describe the next-nearest hopping t_2. The primitive vectors $\vec{a}_1$, $\vec{a}_2$, and $\vec{a}_3$ are chosen along the O_x, O_y, and O_z directions.

First, let us notice that, in the semimetallic case $t_2 = 0$, there is a *chiral* operator $\Gamma = \sigma_z \otimes \sigma_z$, where σ_z is the Pauli matrix. The anticommutation of this operator with the Hamiltonian $[H, \Gamma]_+ = 0$ ensures that the energy spectrum is symmetric around zero energy. That is, for any momentum $\vec{k}$, one finds in the spectrum a pair of energies $(E_{\vec{k}}, -E_{\vec{k}})$.

Another symmetry present in the semimetallic case is the *inversion* defined by $U_I = \sigma_x \otimes \sigma_x$. Under this operation, the Hamiltonian transforms as $U_I H(\vec{k}, \gamma, \gamma_\perp) U_I^{-1} = H(-\vec{k}, \gamma, \gamma_\perp)$, denoting the spectral symmetry $E(\vec{k}, \gamma, \gamma_\perp) = E(-\vec{k}, \gamma, \gamma_\perp)$.

Concerning the TR symmetry, this would involve $H(\vec{k}, \gamma, \gamma_\perp) = H^*(-\vec{k}, \gamma, \gamma_\perp)$, but in the presence of the magnetic phases $\gamma, \gamma_\perp$, our system does not obey this symmetry.

The energy spectrum for different parameters is shown in Fig. 2, where many degenerate eigenenergies can be observed. According to Ref. [31], any twofold degeneracy implies the existence of an antiunitary operator that commutes with the Hamiltonian at the degeneracy points. In our case, we find four such antiunitary operators, which are presented in Table I (where σ_x and σ_y are Pauli matrices, and K represents the complex conjugation).

In Table I, we show the antiunitary operators Ω_i with $(i = 1, \ldots, 4)$ which, under the parameters in the second column, protect the degenerate points in the k space indicated in the next column. As an illustration, in the semimetallic case exhibited in Fig. 2(a), the operator Ω_1 protects the band touching at $k_x = 0, k_y = \pm\pi$ (and also $k_x = \pm\pi, k_y = 0$), for any k_z in the range $[-\pi, \pi)$. In the insulating case from Fig. 2(b), the same operator Ω_1 protects the degeneracy of the two conduction subbands (and valence subbands as well) at the set of points $(k_x = \pm\pi, k_y = \pm\pi, \forall k_z)$. The operators Ω_2 and Ω_3 protect the degeneracies in the semimetallic systems

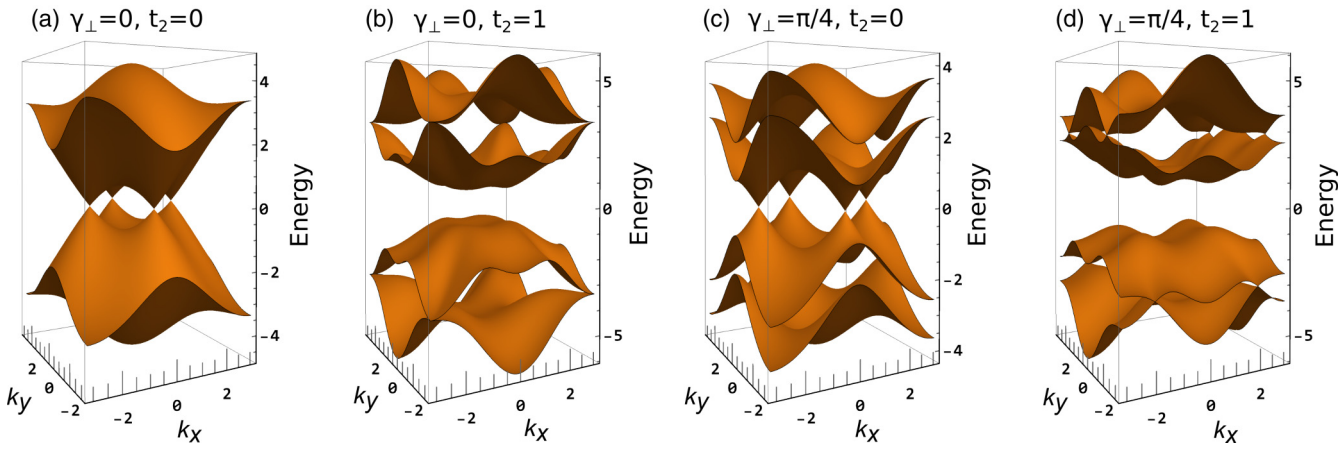

FIG. 2. The energy spectrum is depicted for various parameters $(t_2, \gamma_\perp)$ with a fixed momentum $k_z = \pi/4$. When $t_2 = 0$, the system exhibits a semimetallic phase regardless of the value of $\gamma_\perp$ [as illustrated in (a) and (c)]. On the other hand, as shown in (b) and (d), the system undergoes an insulating phase when t_2 is present.

with $\gamma_\perp \neq 0$ at two different values of k_z (namely, $k_z = 0$ and $k_z = \pm\pi$). Finally, the antiunitary operator Ω_4 refers to the degeneracies in the four subbands existing in the insulating case $t_2 \neq 0$ at $kz = \pm\pi$.

One has to mention that these four operators do not protect all the degenerate points observed in Fig. 2, meaning that some other symmetries may be involved.

Remember that the spectra in Fig. 2 are calculated at fixed $k_z = \pi/4$. In what follows, k_z is a variable, and we look for the *locus* of the points in the Brillouin zone for which $E(k_x, k_y, k_z) = 0$. That is, we look for the points where the band touching occurs in the semimetallic phase. Obviously, these points occur when $\det|H(\vec{k})| = 0$, where $H(\vec{k})$ is given by Eq. (2). This constraint can be satisfied only for $t_2 = 0$, i.e., in the absence of the next nearest hopping. Then the resulting expression of the constraint becomes

$$k_z = \pm\cos^{-1}[2\cos(k_x) + 2\cos(k_y) - \cos(2\gamma_\perp) + 2i\sin(k_x)\sin(k_y)]. \quad (4)$$

Since k_z should be real, the last term in the above equation must be zero, and there are several possibilities to cancel that term: either $k_x = 0, \pm\pi$ or $k_y = 0, \pm\pi$. In what follows, we observe two distinct cases depending on $\gamma_\perp$. Thus, for $\gamma_\perp = 0$ and $k_x = 0$, Eq. (4) turns into

$$k_z = \pm\cos^{-1}(1 + 2\cos k_y), \quad (5)$$

which describes the curves in Fig. 3(a), showing the locus of the touching points in the semimetallic system in the absence of the perpendicular phase $\gamma_\perp$. For $\gamma_\perp \neq 0$, the behavior is different, as can be seen in Fig. 3(b), where with the choice $\gamma_\perp = \pi/4$, the constraint equation becomes

$$k_z = \pm\cos^{-1}(2 + 2\cos k_y). \quad (6)$$

We notice that, in contrast with the previous case $\gamma_\perp = 0$, the value $k_x = 0$ is no longer a solution at $k_z = \pm\pi$, and instead, one gets $k_x = \pm\pi/3$. Then the value $k_y = \pm\pi$ becomes compulsory to cancel the imaginary part of Eq. (4). This situation creates two branches in the (k_x, k_z) plane, which with increasing k_z merge into the point $(k_x = 0, k_y = \pm\pi, k_z = \pm\pi/2)$, as can be observed in Fig. 3(b). The concept is that the introduction of $\gamma_\perp$ leads to the bifurcation of the locus in the momentum space.

In what follows, we shall examine how surface and hinge states emerge in finite systems with different geometries.

III. SURFACE AND HINGE STATES FOR SLAB AND NANOWIRE SYSTEMS

In this section, we study finite systems with two kinds of geometry, namely, the slabs and wires. The objective is to demonstrate under what conditions the presence of the margins induces topological states of the surface and hinge types.

The slab consists of two infinite planes parallel to the (O_x, O_z) axis separated by a finite distance which comprises an integer number M of unit cells along the O_y axis. The intention is to make evident surface states for two kinds of slabs with different interconnection of the atoms at the edges which are obtained by different tailoring. For the first slab, the front

TABLE I. The antiunitary operators Ω_i that protect the degenerate points in k space for the parameters listed in the second column.

Antiunitary operator	Parameters	Degenerate points (k_x, k_y, k_z)
$\Omega_1 = i(\sigma_x \otimes \sigma_y)K$	$t_2 = 0, \gamma_\perp = 0$	$[0, \pm\pi, k_z \in (-\pi, \pi)]$, $[\pm\pi, 0, k_z \in (-\pi, \pi)]$
	$t_2 \neq 0, \gamma_\perp = 0$	$[\pm\pi, \pm\pi, k_z \in (-\pi, \pi)]$
$\Omega_2 = i(\sigma_0 \otimes \sigma_y)K$	$t_2 = 0, \gamma_\perp \neq 0$	$(0, \pm\pi, 0)$, $(\pm\pi, 0, 0)$
$\Omega_3 = i(\sigma_y \otimes \sigma_x)K$	$t_2 = 0, \gamma_\perp \neq 0$	$[k_x \in (-\pi, \pi), 0, \pm\pi]$, $[0, k_y \in (-\pi, \pi), \pm\pi]$
$\Omega_4 = i(\sigma_y \otimes \sigma_0)K$	$t_2 \neq 0, \gamma_\perp = 0$	$(k_x = k_y, k_y = k_x, \pm\pi)$

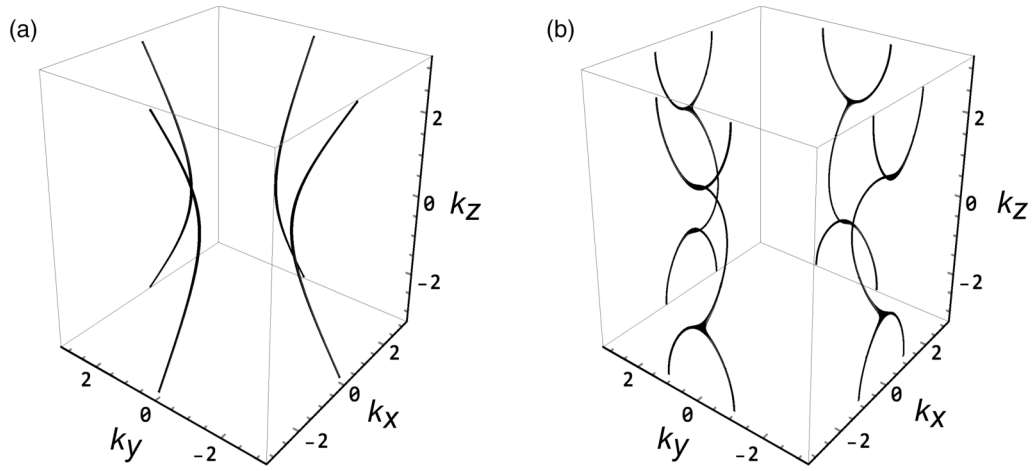

FIG. 3. The locus of the band-touching points for the semimetallic case $t_2 = 0$ (a) in the absence of $\gamma_\perp = 0$ and (b) in the presence of $\gamma_\perp = \pi/4$.

plane contains only atoms of the types A and C, while the back plane contains B and D atoms. Such a structure will be called an AC/BD slab. The second one is rotated by $\pi/4$ (i.e., it is oriented along $\vec{a}_1 + \vec{a}_2$) compared with the first one, in which case the geometry ensures that both the front and back planes contain all four atoms A, B, C, and D. This configuration will be called ABCD/ABCD.

The energy spectra as a function of k_x and k_z (which remain good quantum numbers) are obtained by the numerical diagonalization of the Hamiltonians corresponding to the two slab structures. For example, if we choose the O_x axis along the $\vec{a}_1$ direction and the O_z axis along the $\vec{a}_3$ direction, by imposing vanishing boundary conditions on the O_y direction, we get the Hamiltonian of the AC/BD slab:

$$
\begin{aligned}
H(k_x, m, k_z, \gamma, \gamma_\perp) &= H_1(k_x, m, k_z, \gamma) + H_2(k_x, m, k_z, \gamma) + H_\perp(k_x, m, k_z, \gamma_\perp);\\
H_1(k_x, m, k_z, \gamma) &= t_1 \sum_m [\exp(-i\gamma) + \exp(i\gamma - ik_x)] a^\dagger_{k_x,m,k_z} b_{k_x,m,k_z} + [\exp(i\gamma) + \exp(-i\gamma - ik_x)] a^\dagger_{k_x,m,k_z} b_{k_x,m-1,k_z} + \text{H.c.}\\
&\quad + t_2 \sum_m 2\cos(k_x)\left[a^\dagger_{k_x,m,k_z} a_{k_x,m,k_z} - b^\dagger_{k_x,m,k_z} b_{k_x,m,k_z}\right] - t_2 \sum_m \left[a^\dagger_{k_x,m,k_z} a_{k_x,m+1,k_z} - b^\dagger_{k_x,m,k_z} b_{k_x,m+1,k_z} + \text{H.c.}\right],\\
H_2(k_x, m, k_z, \gamma) &= H_1(a \mapsto c, b \mapsto d, \gamma \mapsto -\gamma);\\
H_\perp(k_x, m, k_z, \gamma_\perp) &= t_\perp \sum_m [\exp(i\gamma_\perp) + \exp(-i\gamma_\perp + ik_z)] a^\dagger_{k_x,m,k_z} c_{k_x,m,k_z} + [\exp(-i\gamma_\perp) + \exp(i\gamma_\perp + ik_z)] b^\dagger_{k_x,m,k_z} d_{k_x,m,k_z} + \text{H.c.}
\end{aligned}
\tag{7}
$$

A similar Hamiltonian can also be written for the ABCD/ABCD slab.

We focus first on the semimetallic cases characterized by $(t_2 = 0, \gamma_\perp = 0)$ and $(t_2 = 0, \gamma_\perp \neq 0)$. The vanishing of t_2 ensures the bipartitism of the lattice and automatically guarantees the electron-hole symmetry in the spectrum [32]. In Fig. 4, we show four different semimetallic spectra corresponding to the two slab structures with/without the vertical phase $\gamma_\perp$. Notably, it is to observe the presence of a flat band at $E = 0$ in the AC/BD structure, independently of the value of the phase $\gamma_\perp$ [see Figs. 4(a) and 4(b)]. In what follows, we provide analytical evidence that the flat band supports surface states which manifest themselves by localization along the direction perpendicular to the surfaces at fixed momenta k_x, k_z.

We look for the eigenfunctions of the Hamiltonian in Eq. (7) as

$$
|\psi(k_x, k_z, \gamma, \gamma_\perp)\rangle = \sum_m \left(\alpha^{\text{A}}_{k_x,m,k_z} a^\dagger_{k_x,m,k_z} + \alpha^{\text{B}}_{k_x,m,k_z} b^\dagger_{k_x,m,k_z} + \alpha^{\text{C}}_{k_x,m,k_z} c^\dagger_{k_x,m,k_z} + \alpha^{\text{D}}_{k_x,m,k_z} d^\dagger_{k_x,m,k_z}\right)|0\rangle. \tag{8}
$$

From $H(k_x, m, k_z, \gamma, \gamma_\perp)|\psi(k_x, k_z, \gamma, \gamma_\perp)\rangle = E(k_x, k_z)|\psi(k_x, k_z, \gamma, \gamma_\perp)\rangle$, in the semimetallic scenario, the coefficients $\alpha^{\text{A}}_{k_x,m,k_z}$, $\alpha^{\text{B}}_{k_x,m,k_z}$, $\alpha^{\text{C}}_{k_x,m,k_z}$, and $\alpha^{\text{D}}_{k_x,m,k_z}$ satisfy the following set of equations:

$$
\begin{aligned}
X(\gamma, k_x)\alpha^{\text{B}}_{k_x,m,k_z} + X(-\gamma, k_x)\alpha^{\text{B}}_{k_x,m-1,k_z} + t_\perp h(\gamma_\perp, -k_z)\alpha^{\text{C}}_{k_x,m,k_z} &= E(k_x, k_z)\alpha^{\text{A}}_{k_x,m,k_z},\\
X^*(\gamma, k_x)\alpha^{\text{A}}_{k_x,m,k_z} + X^*(-\gamma, k_x)\alpha^{\text{A}}_{k_x,m+1,k_z} + t_\perp h(-\gamma_\perp, -k_z)\alpha^{\text{D}}_{k_x,m,k_z} &= E(k_x, k_z)\alpha^{\text{B}}_{k_x,m,k_z},
\end{aligned}
$$

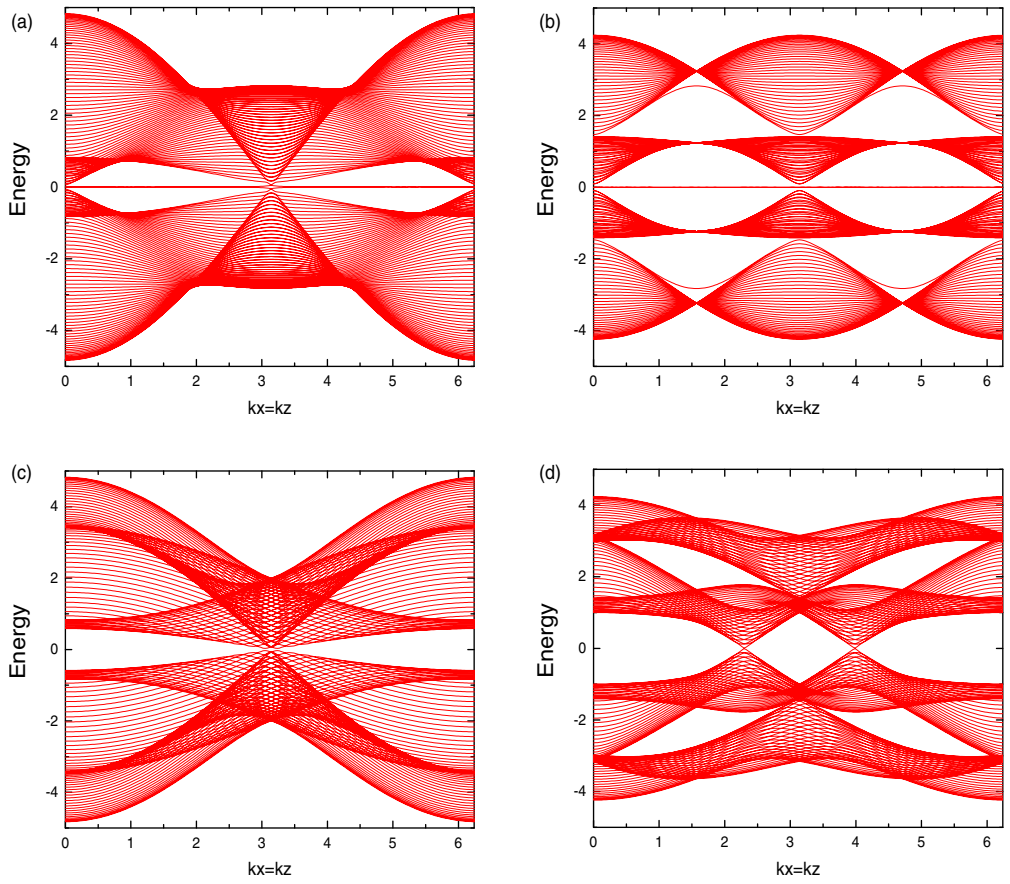

FIG. 4. Semimetallic energy spectra ($t_2 = 0$, $t_\perp = 1$) for two slab geometries: (a) AC/BD with $\gamma_\perp = 0$, (b) AC/BD with $\gamma_\perp = \pi/4$, (c) ABCD/ABCD with $\gamma_\perp = 0$, and (d) ABCD/ABCD with $\gamma_\perp = \pi/4$. In the AC/BD case, a prominent flat zero-energy band is observed, regardless of the $\gamma_\perp$ phase.

$$
\begin{aligned}
X(-\gamma, k_x)\alpha^{\mathrm{D}}_{k_x,m,k_z} + X(\gamma, k_x)\alpha^{\mathrm{D}}_{k_x,m-1,k_z} + t_\perp h(-\gamma_\perp, k_z)\alpha^{\mathrm{A}}_{k_x,m,k_z} &= E(k_x, k_z)\alpha^{\mathrm{C}}_{k_x,m,k_z},\\
X^*(-\gamma, k_x)\alpha^{\mathrm{C}}_{k_x,m,k_z} + X^*(\gamma, k_x)\alpha^{\mathrm{C}}_{k_x,m+1,k_z} + t_\perp h(\gamma_\perp, k_z)\alpha^{\mathrm{B}}_{k_x,m,k_z} &= E(k_x, k_z)\alpha^{\mathrm{D}}_{k_x,m,k_z},
\end{aligned}
\tag{9}
$$

with the parameter $X(\gamma, k_x) = t_1[\exp(-i\gamma) + \exp(i\gamma - ik_x)]$ and $h(\gamma_\perp, k_z) = \exp(i\gamma_\perp) + \exp(-i\gamma_\perp - ik_z)$.

In what follows, we prove that the hopping amplitude $t_\perp$, which defines the vertical interconnection in the 3D structure, plays an important role concerning the localization of the topological states at $E = 0$. However, it is helpful to first look at the localization properties when the interlayer hopping amplitude is deliberately set to zero ($t_\perp = 0$), in which case $h(\gamma_\perp, k_z)$ in Eq. (9) is canceled, and the k_z dependence is removed. Consequently, the Hamiltonian becomes block diagonal and describes two distinct 2D layers, which only differ by the sign of the in-plane phase parameter γ. Each layer is in fact an infinite ribbon along the O_x direction and of finite width along the O_y direction. Remember that the lower layer is occupied by A and B atoms, while the upper one is occupied by the C and D atoms. The pair of ribbons presents a zero-energy flat band. All four equations in Eq. (9) decouple, and by applying the boundary conditions $\alpha^{\mathrm{B}}_{k_x,0,k_z} = \alpha^{\mathrm{A}}_{k_x,M+1,k_z} = 0$ and $\alpha^{\mathrm{D}}_{k_x,0,k_z} = \alpha^{\mathrm{C}}_{k_x,M+1,k_z} = 0$, one can determine the coefficients of the wave function associated with the zero eigenvalues:

$$
\begin{aligned}
\alpha^{\mathrm{A}}_{k_x,m} &= \left[-\frac{X^*(\gamma, k_x)}{X^*(-\gamma, k_x)}\right]^{m-1}\alpha^{\mathrm{A}}_{k_x,1},\\
\alpha^{\mathrm{B}}_{k_x,m} &= \left[-\frac{X(\gamma, k_x)}{X(-\gamma, k_x)}\right]^{M-m}\alpha^{\mathrm{B}}_{k_x,M},\\
\alpha^{\mathrm{C}}_{k_x,m} &= \left[-\frac{X^*(-\gamma, k_x)}{X^*(\gamma, k_x)}\right]^{m-1}\alpha^{\mathrm{C}}_{k_x,1},\\
\alpha^{\mathrm{D}}_{k_x,m} &= \left[-\frac{X(-\gamma, k_x)}{X(\gamma, k_x)}\right]^{M-m}\alpha^{\mathrm{D}}_{k_x,M}.
\end{aligned}
\tag{10}
$$

It results immediately that the wave function $|\Psi^{\mathrm{A}}(k_x)\rangle = \Sigma_m \alpha^{\mathrm{A}}_{k_x,m}|a^\dagger_{k_x,m}|0\rangle$ is a topological eigenfunction localized at the edge $m = 1$ if $|X(\gamma, k_x)/X(-\gamma, k_x)| < 1$. Instead, the function $|\Psi^{\mathrm{B}}(k_x)\rangle$, defined similarly, is localized at the other edge $m = M$. The two functions $|\Psi^{\mathrm{C}}(k_x)\rangle$ and

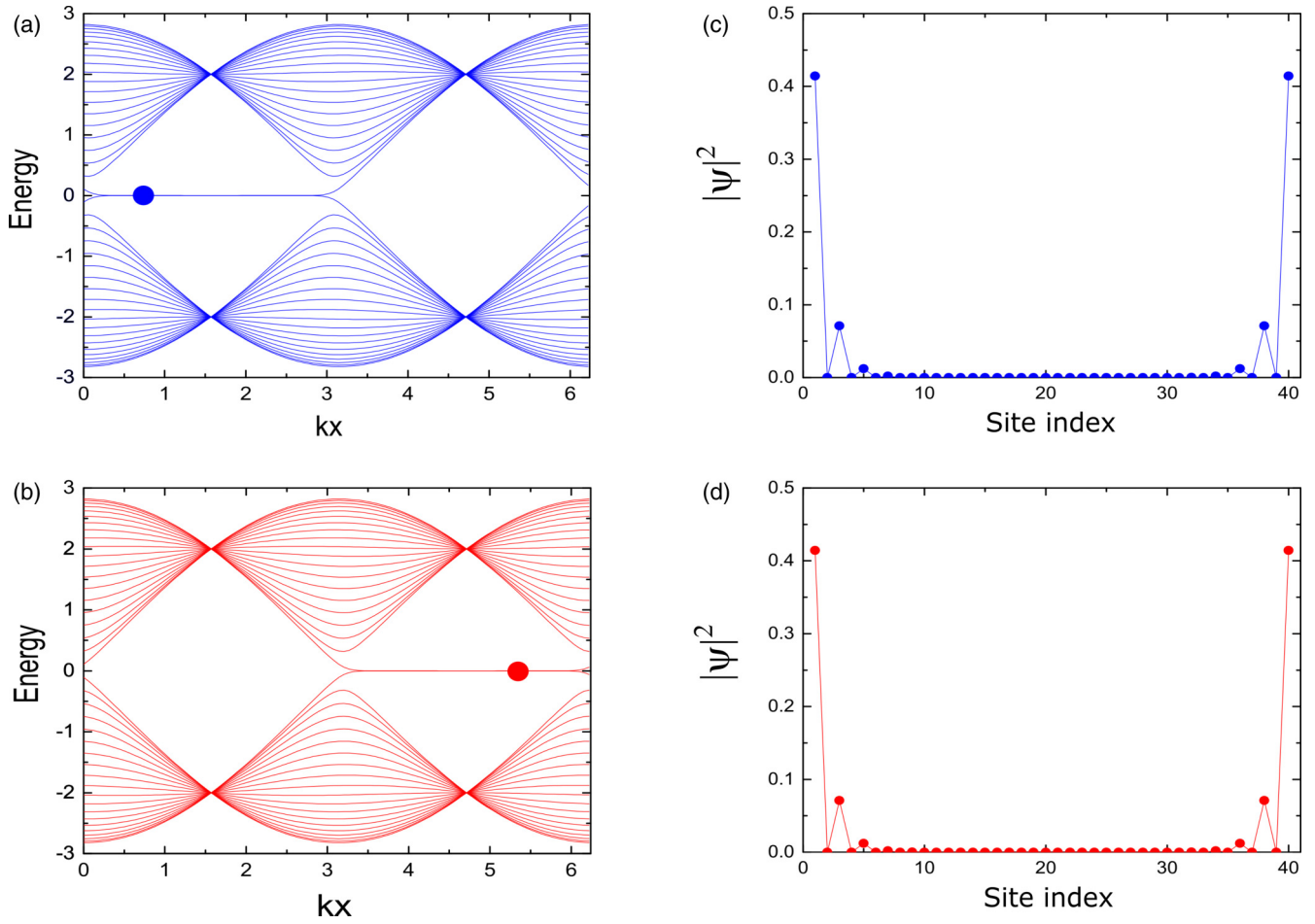

FIG. 5. (a) and (b) The energy spectra are shown for two independent ribbons ($t_2 = 0$, $t_\perp = 0$). Both ribbons are oriented along the $\vec{a}_1$ direction, as depicted in Fig. 1. The red ribbon is made of A, B atoms, while the blue ribbon consists of C, D atoms, the only difference being the sign of γ. In (c) and (d), we illustrate the spatial localization of the wave functions with zero energy for two values of k_x corresponding to the red and blue points. It is evident that the localization remains the same in the two cases.

$|\Psi^{\mathrm{D}}(k_x)\rangle$ present the same localization but with the condition $|X(-\gamma, k_x)/X(\gamma, k_x)| < 1$. Obviously, the two conditions cannot be fulfilled simultaneously at a given k_x. However, the first condition can be satisfied for $k_x \in (\pi, 2\pi)$ and the second for $k_x \in (0, \pi)$, as shown in Figs. 5(a) and 5(b). The spatial confinement of the wave function associated with the $E(k_x) = 0$ eigenvalue can be examined by evaluating $|\langle\Psi(k_x)|i\rangle|^2$, $i =$ site index, which represents the projection of the wave function $|\Psi(k_x)\rangle$ onto the sites across the width. This calculation validates the edge localization for each 2D layer, as shown in Figs. 5(c) and 5(d).

In the 3D case, still paying attention to the semimetallic case $t_2 = 0$, we note that the parameter $t_\perp$ is different from zero, while the vertical phase $\gamma_\perp$ can be both zero or nonzero depending on the context. The dependence on k_z is restored, so that the eigenenergies now depend on both k_x and k_z. The energy spectra corresponding to the two previously introduced slab terminations (AC/BD and ACBD/ACBD) are shown in Fig. 4. It is noteworthy that the zero-energy flat bands are also present in the 3D case but only in the AC/BD configuration, no matter the value of the perpendicular flux $\gamma_\perp$. Comparing with the scenario discussed above where $t_\perp = 0$, the localization at the margins of the system has distinct properties.

In what follows, we look for *surface states* associated with the energy $E(k_x, k_z) = 0$. We start again from Eq. (9) and use the ansatz $\alpha^{(j)}_{k_x,m,k_z} = \lambda^{m-1}_{(j)}\alpha^{(j)}_{kx,1,k_z}$ and $\alpha^{(j)}_{k_x,m,k_z} = \lambda^{M-m}_{(j)}\alpha^{(j)}_{kx,M,k_z}$, where j stands for A, B, C, or D, and m is the site index along the O_y direction. Obviously, for the existence of the surface states, it is imperative that the condition $|\lambda_{(j)}| < 1$ be met. This condition guarantees that the states reach their peak amplitudes at the boundaries and decay within the bulk of the structure. The coefficients $\lambda_{(j)}$ satisfy quadratic equations and the properties $\lambda_{\mathrm{A}} = \lambda_{\mathrm{D}}$, $\lambda_{\mathrm{B}} = \lambda_{\mathrm{C}}$, as demonstrated in Appendix B.

The aspect of the spatial distribution of the wave function, obtained by the numerical calculation of the local density of states $|\langle\Psi(k_x, k_z)|i\rangle|^2$, reveals important differences compared with the case $t_\perp = 0$ and depends qualitatively by $\gamma_\perp$. The result of the analytical calculation for the localization on the first and last cell of the AC/BD structure is given by Eq. (B5), whereas the numerical results, which agree with the analytical ones, are shown in Fig. 6. For $\gamma_\perp = 0$, in the first cell ($m = 1$), both sites B (in the lower layer) and C

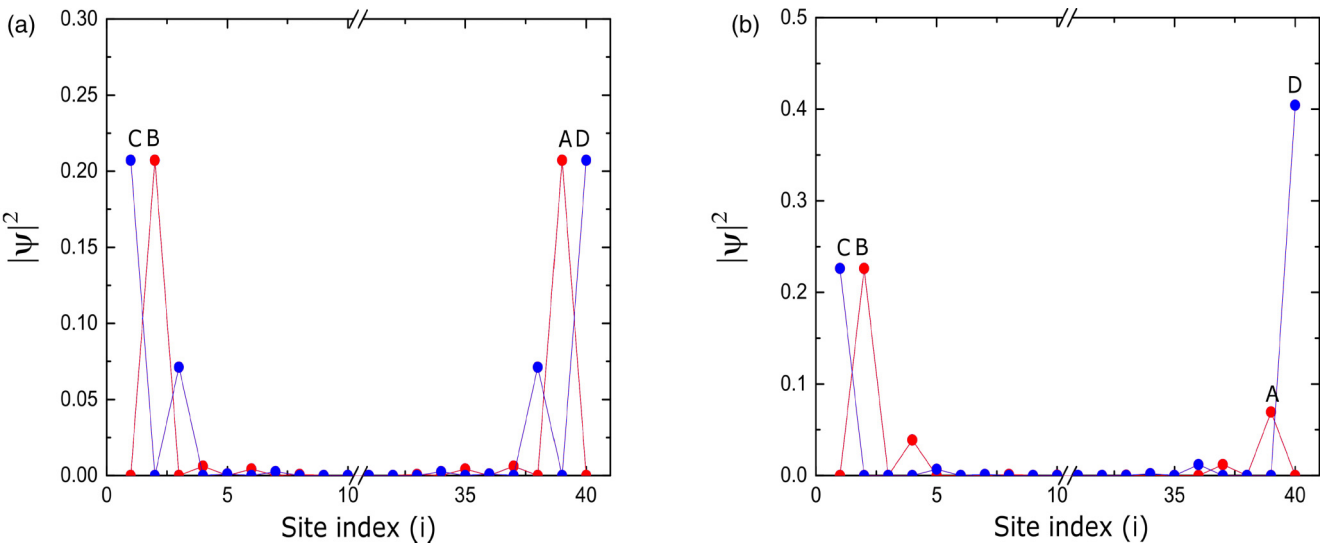

FIG. 6. The spatial distribution of two zero-energy wave functions is illustrated, considering hopping amplitudes $t_2 = 0$ and $t_\perp = 1$. Red signifies localization on the first layer, comprised of A and B sites, while blue indicates localization on the second layer, consisting of C and D sites. In (a), $\gamma_\perp = 0$, whereas in (b), $\gamma_\perp = \pi/4$. The calculations are performed at $k_x = k_z = \pi/4$.

(in the upper layer) are equally occupied. At the opposite boundary, in the last cell ($m = M$), sites A and D behave similarly. The outcome is counterintuitive for this geometry, defying expectations that suggest an occupancy pattern of the A, C, and B, D sites due to their direct connection through $t_\perp$. This one-site shift, occurring at the edges, is analytically confirmed by Eq. (B5) and is unaffected by parameters $t_\perp$ and $\gamma_\perp$. Another significant effect arises from the inversion symmetry

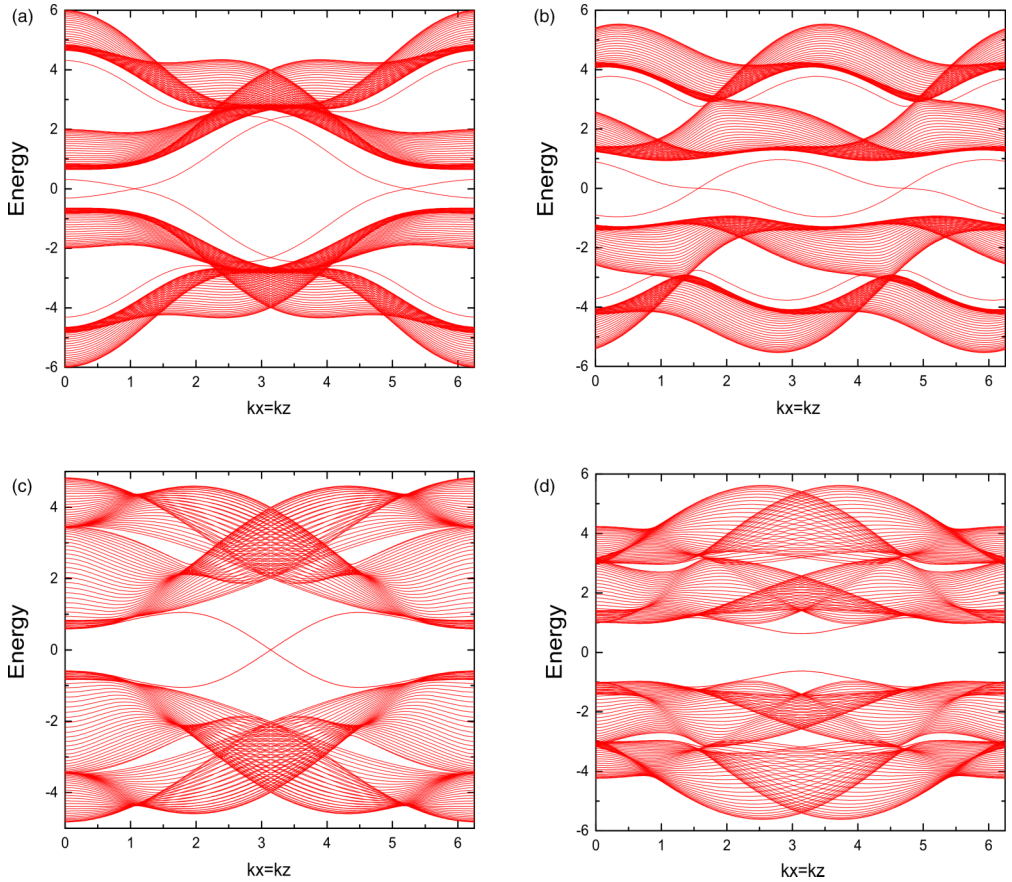

FIG. 7. The energy spectrum for two systems with slab geometry ($t_2 = 1$, $t_\perp = 1$): AC/BD with phases (a) $\gamma_\perp = 0$ and (b) $\gamma_\perp = \pi/4$, ABCD/ABCD with phases (c) $\gamma_\perp = 0$ and (d) $\gamma_\perp = \pi/4$. In all cases, the bulk gap is populated with dispersive surface states.

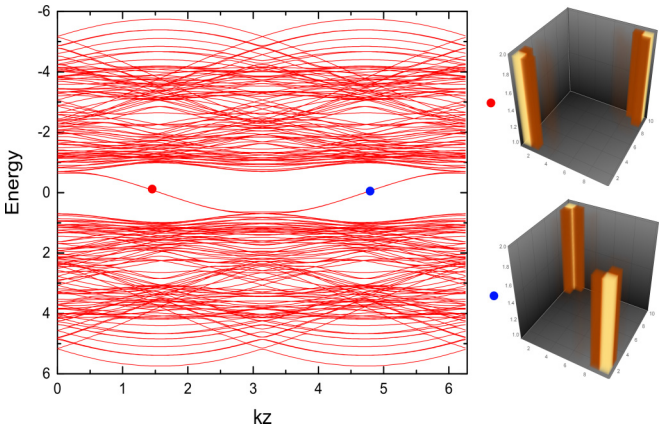

FIG. 8. Left: Energy spectrum of the nanowire system in the second-order topological insulator (SOTI) phase. Red and blue points represent intersections of the gapless hinge states with the Fermi level. Right: The eigenfunctions corresponding to the red and blue intersections demonstrate the one-dimensional nature of the hinge states. The system consists of a 10×10 unit cells lattice in both the O_x and O_y directions, with $t_2 = 1$, $t_\perp = 1$, and $\gamma_\perp = \pi/4$.

breaking induced by $\gamma_\perp$ in the AC/BD structure. The absence of the inversion results in an asymmetry of the wave function at the two ends, as depicted in Fig. 6(b), and confirmed by Eq. (B5).

In the presence of the nonzero next nearest hopping ($t_2 \neq 0$), the energy spectrum of the slab opens a topological gap, like the one observed for the 3D infinite system in Fig. 2. The difference consists, however, of the appearance of gapless *dispersive* surface states, which can be noticed in Fig. 7 for both types of slab geometry (i.e., AC/BD and ABCD/ABCD). There are nevertheless several peculiarities: (i) the AC/BD structure exhibits two degeneracy points of the topological surface states at $E = 0$ independently of the flux $\gamma_\perp$, (ii) on the other hand, in the ABCD/ABCD structure, $\gamma_\perp$ is essential as the degeneracy occurs either in one point or none. The second case shown in Fig. 7(d) is the most interesting, as it exhibits a surface gap that may accommodate hinge states in case the slab is transformed into a nanowire (the surface gap is also predicted in a continuum model in Ref. [33]). This would prove the possibility to create a SOTI by stacking diatomic layers with Chern properties. *Chiral hinge states* are anticipated to be generated via the interlayer connection and the related phase $\gamma_\perp$. One would expect the 3D QAHE to occur in this kind of system. The details of these expectations will be discussed in what follows.

To verify this, we need to create a nanowire, which requires applying hard-wall boundary conditions also in the O_x direction, while maintaining the same ABCD geometry on the surface. Consequently, the energy spectrum becomes only dependent on the k_z momentum. The energy spectrum is calculated under the conditions where the energy gap reaches its maximum: $t_2 = 1$, $t_\perp = 1$, and $\gamma_\perp = \pi/4$. Our anticipation regarding the presence of chiral hinge states is confirmed in Fig. 8 (on the left), as the gap in the energy spectrum is filled with gapless states. To confirm the 1D character of these states, we numerically calculate the local density of states $|\langle \Psi(k_z)|n, m\rangle|^2$, where n and m index the unit cells in the O_x and O_y directions, and the result is presented in Fig. 8 (on the right).

By setting the Fermi level in the middle of the gap, one reveals two intersections at specific k_z values, denoted by red and blue dots. These two degenerate states are running along opposite edges of the wire, as illustrated in Fig. 8 (on the right). Obviously, the velocities $v_k = dE(k_z)/dk_z$ at these two intersections are nonzero. The sign of the derivative provides an indication of currents flowing along the hinges in opposite directions.

In what follows, we face the question of how the hinge channels will be organized to form a closed path in the case of finite 3D structures.

IV. FINITE GEOMETRY: HINGE STATES AND QAHE IN 3D STRUCTURES

In the previous section, we demonstrated that, in the ABCD/ABCD slab geometry, the presence of $\gamma_\perp$ leads to the emergence of a surface gap, as shown in Fig. 7(d). We have also seen that this gap is populated with gapless 1D hinge states if supplementary hard-wall boundaries, which transform the slab into an infinite wire, are imposed Fig. 8.

In this section, we proceed by using hard-wall boundary conditions in all three directions and creating in this way a finite parallelepiped structure. We highlight how the hinge states organize themselves to generate closed chiral paths. These closed chiral paths may support the QAHE in the 3D SOTI structure.

To calculate the Hall effect, one needs to attach four leads, which we arrange in the cross configuration. Obviously, to point out this effect in 3D, two of them (say, the current leads) should be attached to the lower face of the parallelepiped, while the other two leads (necessary to measure the Hall voltage) are attached to the upper face, as in Fig. 9(b). Then the well-known Landauer-Büttiker formalism will be used to calculate the transmission coefficients between the four leads and the Hall resistance.

First, we analyze some structural details which affect the spectral and transport properties of the finite system. By construction, all the lateral sides of the parallelepiped have an ABCD atomic configuration. However, the top and bottom faces present a different arrangement, which contains either A and B or C and D atoms. The number of layers stacked in the structure proves to be essential for the problem. In the case of an odd number of layers, the two faces are identical. On the other hand, for an even number of layers, the bottom and top faces are different (let us choose A-B at the bottom and C-D at the top). In this case, the in-plane γ phase shows the opposite sign on the two faces, and this gives rise to major changes in the trajectory of the hinge states and, consequently, affects the QHE.

Let us examine the energy spectrum and the hinge-type wave functions in terms of the perpendicular phase $\gamma_\perp$ and the number of layers. The result is presented in Fig. 10, where some properties are evident: (i) the electron-hole symmetry, (ii) the periodicity with $\delta\gamma_\perp = \pi$, and (iii) the mirror symmetry around $\gamma_\perp = \pi/2$. Additionally, it is easy to realize that $E(\gamma, \gamma_\perp) = E(-\gamma, -\gamma_\perp)$. However, the striking feature consists of the completely different aspect of the hinge states

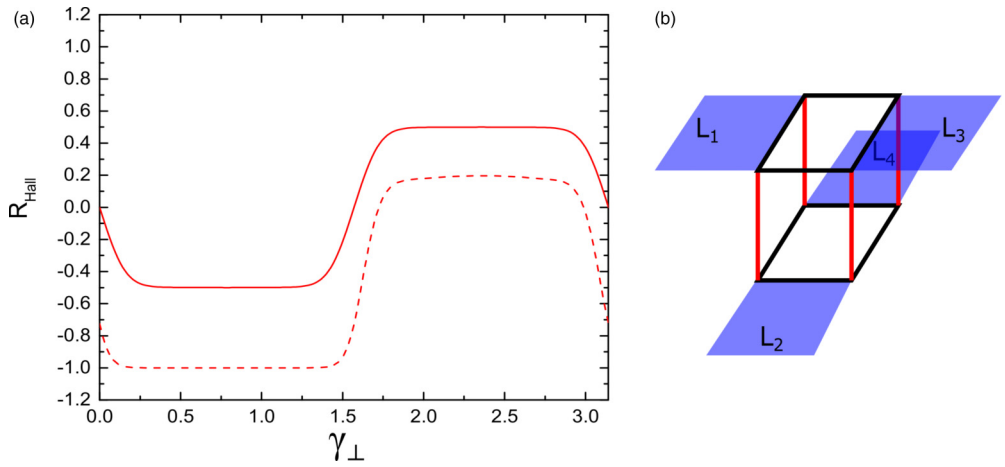

FIG. 9. (a) The Hall resistance is plotted as a function of the perpendicular phase $\gamma_\perp$ in the second-order topological insulator (SOTI) phase ($t_2 = 1$, $t_\perp = 1$, $\gamma = \pi/4$) at the zero Fermi energy. The red solid line represents the case of dimensions $15 \times 15 \times 10$, while the red dashed line corresponds to the case of dimensions $15 \times 15 \times 9$. (b) A sketch of the Hall device with four leads is provided to facilitate a better understanding of the numerical calculations in the cross-lead geometry.

in the two cases which are distinguished by the number of layers. The odd number of layers allows for the chiral circuit shown in Fig. 10(d), which connects all four leads of the Hall device. In the case of an even number of layers, the mismatch between the direction of the in-plane γ phase on the lower and upper faces generates two separate circuits, as in Fig. 10(c). Obviously, in this case, the QHE vanishes, except in the situation when the leads are wide such that they touch both circuits. In this situation, the quantum Hall resistance may become fractional, as we shall see below.

The transmission coefficients $T_{\alpha\beta}$ (where $\alpha, \beta = 1, 2, 3, 4$ are the lead indexes) are computed using the Green's function

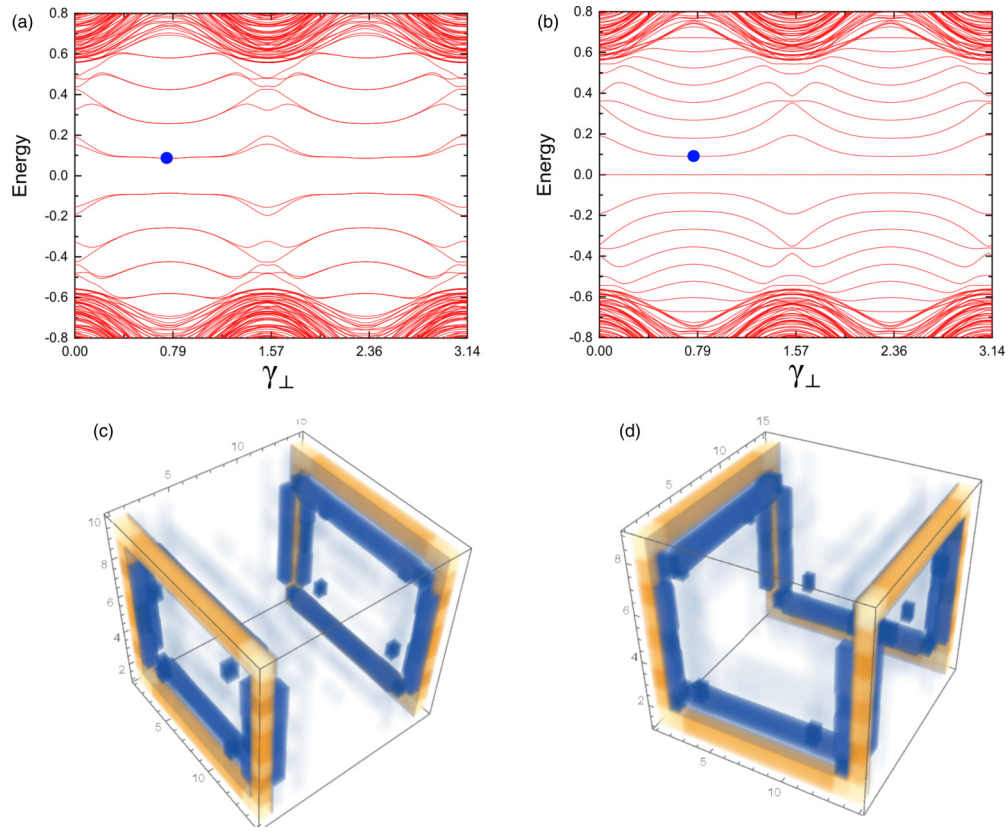

FIG. 10. The eigenenergy spectrum of systems consisting of (a) $15 \times 15 \times 10$ lattice sites in the O_x, O_y, and O_z directions and (b) $15 \times 15 \times 9$ as a function of phase $\gamma_\perp$. The hinge states trajectories are presented in (c) and (d), corresponding to the eigenenergies indicated with blue points in the energy spectra.

approach, which requires not only the sample Hamiltonian in Eq. (1) but also the Hamiltonian terms describing the leads and the lead-sample contacts. Once the transmission coefficients are known, the transverse (Hall) resistance is given by

$$R_H = \frac{T_{23}T_{41} - T_{21}T_{43} - T_{32}T_{14} + T_{12}T_{34}}{2D}, \tag{11}$$

where D is a 3×3 minor of the transmission matrix. The technicalities are explained *in extenso* in Ref. [34] and will not be repeated here.

Even in the absence of an external magnetic field, the Hall effect is expected to be nonzero due to the TR symmetry breaking caused by the intralayer phase γ and interlayer phase $\gamma_\perp$. The dependence of the quantum Hall resistance on $\gamma_\perp$, at fixed $\gamma = \pi/4$, is shown in Fig. 9, where quantum anomalous Hall plateaus can be observed. It is important to remember that the accuracy of the numerically obtained plateaus increases substantially with the size of the system. In our calculation, we use structures consisting of $15 \times 15 \times 9$ and $15 \times 15 \times 10$ sites for the case of the odd and even numbers of layers, respectively.

The only integer plateau occurs for an odd number of layers if $\gamma_\perp \in (0, \pi/2)$. Having in mind that each independent layer is a 2D Chern insulator with $\mathcal{C} = \pm 1$ (depending on the sign of γ) [30], the result $R_H = -1$ in Fig. 9(a) comes out as if we sum the Chern numbers of all the layers. In this case, the transmission matrix is the one specific to the integer QHE, i.e., the matrix T_1 in Eq. (12). This is no longer true if $\gamma_\perp \in (\pi/2, \pi)$, in which case the hinge path in Fig. 10(d) rotates by $C4$, so that the lead connection changes. This situation is described by the transmission matrix T_2, which generates a fractional Hall resistance $R_H = \frac{1}{5}$, as can be noticed in Fig. 9(a).

The same discussion can be resumed for an even number of layers. The key difference comes from the specific shape of the hinge states which show now two disjunct channels, as obvious in Fig. 10(c). This time the involved matrices are T_3 for $\gamma_\perp \in (0, \pi/2)$ and T_4 in the range $(\pi/2, \pi)$, resulting in $R_H = \pm\frac{1}{2}$, as shown in Fig. 9(a) with the red solid line.

$$T_1 = \begin{pmatrix} -1 & 1 & 0 & 0 \\ 0 & -1 & 1 & 0 \\ 0 & 0 & -1 & 1 \\ 1 & 0 & 0 & -1 \end{pmatrix},$$

$$T_2 = \begin{pmatrix} -2 & 0 & 1 & 1 \\ 1 & -2 & 0 & 1 \\ 1 & 1 & -2 & 0 \\ 0 & 1 & 1 & -2 \end{pmatrix}, \tag{12}$$

$$T_3 = \begin{pmatrix} -2 & 1 & 1 & 0 \\ 0 & -1 & 1 & 0 \\ 1 & 0 & -2 & 1 \\ 1 & 0 & 0 & -1 \end{pmatrix},$$

$$T_4 = \begin{pmatrix} -1 & 0 & 0 & 1 \\ 1 & -2 & 0 & 1 \\ 0 & 1 & -1 & 0 \\ 0 & 1 & 1 & -2 \end{pmatrix}. \tag{13}$$

The analysis of the transport properties above provides a method for identifying the closure of the hinge state channels in a cross arrangement of the leads. Furthermore, the distinction between systems with an odd or even number of layers becomes immediately apparent through the measurement of the quantum Hall resistance.

V. CONCLUSIONS

We have developed a 3D tight-binding model that presents the spectral properties of a SOTI and the transport properties of the QAHE. This model is constructed by stacking square diatomic layers, each exhibiting Chern properties, resulting in a 3D structure characterized by four atoms per unit cell. The critical components of this model include the next-nearest-hopping integral t_2, the phase associated with the intralayer hopping process γ, and the phase $\gamma_\perp$ related to the vertical interlayer connections $t_\perp$.

We analyze the spectral properties across three distinct geometries: bulk (i.e., a fully periodic 3D lattice), slab, and wire. Each geometry is distinguished by its specific boundary conditions. Within the bulk geometry, the presence of the next nearest hopping plays an essential role in differentiating between semimetallic and insulating phases. This finding reflects a situation like the 2D case. Our examination reveals the presence of chiral and antiunitary symmetries, leading to electron-hole symmetry and the emergence of degeneracy points in the energy spectrum. Furthermore, we provide analytical insight into the evolution in the momentum space of the touching points locus at zero energy in the semimetallic phase.

In the case of the slab geometry, we conducted an energy spectrum analysis for two specific surface configurations: AC/BD and ABCD/ABCD. For the AC/BD surface geometry, in the semimetallic phase, we provide analytical evidence for the existence of zero-energy surface states and calculate their localization by projecting the wave function onto the boundary sites.

In the ABCD/ABCD slab configuration, we observe the emergence of an energy gap in the surface state spectrum caused by $\gamma_\perp$. When moving to the wire geometry, this gap fills with two pairs of hinge states of opposite chirality. This observation suggests that a 3D QAHE should manifest in finite structures. To confirm this, we attach four leads in a cross configuration [see Fig. 9(b)] and calculate the transverse (Hall) resistance using the Landauer-Büttiker formalism.

Interestingly, the number of layers in the structure significantly impacts the path of the hinge states and, consequently, the characteristics of the QAHE. The systems built up from an odd number of layers exhibit two detached hinge channels, while in the case of an even number of layers, there is only a single hinge channel. These different charge conducting paths influence the observed plateaus of the Hall resistance, leading to the fractional ones.

Several theoretical platforms have been proposed for the realization of the 3D Chern insulators, and we mention the magnetic topological materials (for instance, $MnBi_{2n}Te_{3n+1}$ [35] and $Bi_{2-x}Sm_xSe_3$ [36]), the photonic crystals [37], and the topolectric circuits [38,39]. The experimental evidence of

the QAHE was obtained in thin films of chromium-doped $(BiSb)_2Te_3$ [40] and moiré heterostructure $MoTe_2/WSe_2$ [41]. Our theoretical model, which predicts the QAHE along chiral hinge states in SOTIs, is based on two Haldane-type phases in a cubic structure, and we anticipate that it might be realized by the use of the topolectrical method.

ACKNOWLEDGMENTS

We acknowledge financial support from the Core Program of the National Institute of Materials Physics, granted by the Romanian MCID under Project No. PC2-PN23080202. The fee for open-access publication was supported by Project No. 35PFE/2021, funded by the Romanian Ministry of Research, Innovation and Digitalization.

APPENDIX A: CHERN NUMBER CALCULATION FOR THE 2D DIATOMIC SQUARE LATTICE WITH HALDANE-TYPE PHASE

Our model is built up by stacking 2D layers, which are supposed to show Chern topological properties. The Chern insulating behavior of an individual 2D lattice is provided by the intralayer Haldane-type phase attached to the nearest-neighbor-hopping t_1 combined with the possibility of hopping to the next nearest neighbors (described by the parameter t_2) [29,30].

Here, we show the result of an explicit calculation of the Chern number as a function of the phase γ. The calculation is performed following the method used in Ref. [42]. The result is presented in Fig. 11, where it can be seen that the Chern number equals the quantized numbers ± 1, depending on the sign of the phase γ.

APPENDIX B: ANALYTICAL CALCULATION OF SURFACE STATES LOCALIZATION

In the case of $t_\perp \neq 0$ and $E(k_x, k_z) = 0$, the equations in Eq. (9) generate the following equations for the coefficients $\alpha^{(j)}_{k_x,m,k_z}$ (where m is the cell index, and j is the index of the atoms in the unit cell):

$$\begin{aligned} Z_1\alpha^{(j)}_m + Z_2\alpha^{(j)}_{m+1} + Z_3\alpha^{(j)}_{m-1} = 0, \quad & j = \text{A and D}, \\ Z_1\alpha^{(j)}_m + Z_3\alpha^{(j)}_{m+1} + Z_2\alpha^{(j)}_{m-1} = 0, \quad & j = \text{B and C}, \end{aligned} \tag{B1}$$

[we skip the indexes (k_x, k_z)] with the real coefficients:

$$\begin{aligned} Z_1 &= 4t_1^2[\cos(2\gamma) + \cos(k_x)] \\ &\quad - 2t_\perp^2[\cos(2\gamma_\perp) + \cos(k_z)], \\ Z_2 &= 2t_1^2[1 + \cos(2\gamma + k_x)], \\ Z_3 &= 2t_\perp^2[\cos(2\gamma_\perp) + \cos(k_z)]. \end{aligned} \tag{B2}$$

To prove the localization of the surface states at the ends of the slab, we make the ansatz $\alpha^{(j)}_m = \lambda^{m-1}_{(j)}\alpha^{(j)}_1$ if the wave function is localized at $m = 1$ and $\alpha^{(j)}_m = \lambda^{M-m}_{(j)}\alpha^{(j)}_M$ for the other end $m = M$. Obviously, for $|\lambda_{(j)}| < 1$, the wave function projected on the sites $j =$ A, B, C, and D is localized near the borders of the system. The quantity $\lambda_{(j)}$, which controls the decay of the wave function near the surface $m = 1$, satisfies the following quadratic equations:

$$\begin{aligned} Z_2\lambda^2_{(j)} + Z_1\lambda_{(j)} + Z_3 = 0, \quad & \text{if } j = \text{A and D}, \\ Z_3\lambda^2_{(j)} + Z_1\lambda_{(j)} + Z_2 = 0, \quad & \text{if } j = \text{B and C}, \end{aligned} \tag{B3}$$

and at the opposite end $m = M$, we just need to interchange the equation for (A, D) with the equation for (B, C).

Unexpectedly, the above equations indicate different decays as $\lambda_A = \lambda_D$ differs from $\lambda_B = \lambda_C$. The solutions of Eq. (B3) show that, for a specific range of parameters $(\gamma_\perp, t_\perp; k_x, k_z)$, where $|\lambda_{(j)}| < 1$, the system supports surface states. Let us pay attention to localization of the wave function on the first cell $m = 1$ and last cell $m = M$. Due to the boundary conditions $\alpha^{(j)}_0 = \alpha^{(j)}_{M+1} = 0$, from the equations in Eq. (9), we obtain

$$\begin{aligned} X(\gamma, k_x)\alpha^{\text{B}}_1 + h(\gamma_\perp, -k_z)\alpha^{\text{C}}_1 = 0, \\ X^*(\gamma, k_x)\alpha^{\text{A}}_M + h(-\gamma_\perp, -k_z)\alpha^{\text{D}}_M = 0, \\ X(-\gamma, k_x)\alpha^{\text{D}}_1 + h(-\gamma_\perp, k_z)\alpha^{\text{A}}_1 = 0, \\ X^*(-\gamma, k_x)\alpha^{\text{C}}_M + h(\gamma_\perp, k_z)\alpha^{\text{B}}_M = 0, \end{aligned} \tag{B4}$$

from where

$$\begin{aligned} \frac{|\alpha^{(\text{B})}_1|^2}{|\alpha^{(\text{C})}_1|^2} &= \frac{t_\perp^2}{t_1^2}\frac{1 + \cos(2\gamma_\perp - k_z)}{1 + \cos(2\gamma - k_x)}, \\ \frac{|\alpha^{(\text{A})}_M|^2}{|\alpha^{(\text{D})}_M|^2} &= \frac{t_\perp^2}{t_1^2}\frac{1 + \cos(2\gamma_\perp + k_z)}{1 + \cos(2\gamma - k_x)}, \\ \frac{|\alpha^{(\text{D})}_1|^2}{|\alpha^{(\text{A})}_1|^2} &= \frac{t_\perp^2}{t_1^2}\frac{1 + \cos(2\gamma_\perp - k_z)}{1 + \cos(2\gamma + k_x)}, \\ \frac{|\alpha^{(\text{C})}_M|^2}{|\alpha^{(\text{B})}_M|^2} &= \frac{t_\perp^2}{t_1^2}\frac{1 + \cos(2\gamma_\perp + k_z)}{1 + \cos(2\gamma + k_x)}. \end{aligned} \tag{B5, B6}$$

Now by utilizing the same momentum parameters in the slab geometry as in Fig. 6 ($k_x = k_z = \pi/4$), the condition $|\lambda_{(j)}| < 1$ implies that the surface states on sites (B, C) are localized at $m = 1$ and on sites (A, D) at $m = M$. In this

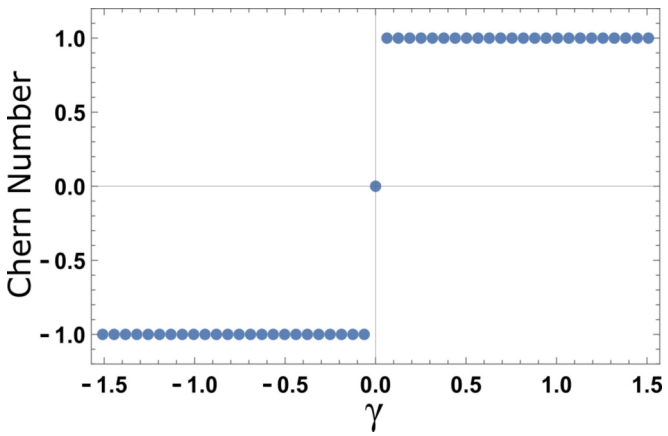

FIG. 11. Chern number as a function of the intralayer phase γ for a two-dimensional (2D) diatomic square lattice. The Chern number takes on quantized values of ± 1 depending on the sign of the phase γ.

scenario, the ratios of endsite localization are described by Eq. (B5). If the momentum parameters are shifted by $3\pi/2$ (i.e., $k_x = k_z = 7\pi/4$), the discussions above remain valid, and the ratios of endsite localization are presented in Eq. (B6).

For the set of values considered in Fig. 6(a), the ratios $|\alpha_1^{(B)}|^2/|\alpha_1^{(C)}|^2 = 1$ and $|\alpha_M^{(A)}|^2/|\alpha_M^{(D)}|^2 = 1$, which match the ratio obtained numerically in the absence of $\gamma_\perp$. In the presence of $\gamma_\perp$ ($\gamma_\perp = \pi/4$), the localization at the boundaries changes, and the projection onto the end sites satisfy the relations $|\alpha_1^{(B)}|^2/|\alpha_1^{(C)}|^2 = 1$ and $|\alpha_M^{(A)}|^2/|\alpha_M^{(D)}|^2 = (\sqrt{2}-1)/(\sqrt{2}+1)$, as observed in Fig. 6(b).

[1] J. Langbehn, Y. Peng, L. Trifunovic, F. von Oppen, and P. W. Brouwer, Reflection-symmetric second-order topological insulators and superconductors, Phys. Rev. Lett. **119**, 246401 (2017).

[2] Z. Song, Z. Fang, and C. Fang, $(d-2)$-dimensional edge states of rotation symmetry protected topological states, Phys. Rev. Lett. **119**, 246402 (2017).

[3] W. A. Benalcazar, B. A. Bernevig, and T. L. Hughes, Electric multipole moments, topological multipole moment pumping, and chiral hinge states in crystalline insulators, Phys. Rev. B **96**, 245115 (2017).

[4] I. A. Nechaev, R. C. Hatch, M. Bianchi, D. Guan, C. Friedrich, I. Aguilera, J. L. Mi, B. B. Iversen, S. Blügel, P. Hofmann *et al.*, Evidence for a direct band gap in the topological insulator Bi_2Se_3 from theory and experiment, Phys. Rev. B **87**, 121111(R) (2013).

[5] M. Eschbach, M. Lanius, C. Niu, E. Młyńczak, P. Gospodarič, J. Kellner, P. Schüffelgen, M. Gehlmann, S. Döring, E. Neumann *et al.*, Bi_1Te_1 is a dual topological insulator, Nat. Commun. **8**, 14976 (2017).

[6] N. Avraham, A. K. Nayak, A. Steinbok, A. Norris, H. Fu, Y. Sun, Y. Qi, L. Pan, A. Isaeva, A. Zeugner *et al.*, Visualizing coexisting surface states in the weak and crystalline topological insulator Bi_2TeI, Nat. Mater. **19**, 610 (2020).

[7] R. Noguchi, M. Kobayashi, Z. Jiang, K. Kuroda, T. Takahashi, Z. Xu, D. Lee, M. Hirayama, M. Ochi, T. Shirasawa *et al.*, Evidence for a higher-order topological insulator in a three-dimensional material built from van der Waals stacking of bismuth-halide chains, Nat. Mater. **20**, 473 (2021).

[8] N. Shumiya, M. S. Hossain, J. X. Yin, Z. Wang, M. Litskevich, C. Yoon, Y. Li, Y. Yang, Y.-X. Jiang, G. Cheng *et al.*, Evidence of a room-temperature quantum spin Hall edge state in a higher-order topological insulator, Nat. Mater. **21**, 1111 (2022).

[9] H. Xue, Y. Yang, F. Gao, and B. Zhang, Acoustic higher-order topological insulator on a kagome lattice, Nat. Mater. **18**, 108 (2019).

[10] H. Xue, Y. Ge, H. X. Sun, Q. Wang, D. Jia, Y.-J. Guan, S.-Q. Yuan, Y. Chong, and B. Zhang, Observation of an acoustic octupole topological insulator, Nat. Commun. **11**, 2442 (2020).

[11] W. Zhu, W. Deng, Y. Liu, J. Lu, H.-X. Wang, Z.-K. Lin, X. Huang, J.-H. Jiang, and Z. Liu, Topological phononic metamaterials, Rep. Prog. Phys. **86**, 106501 (2023).

[12] Y. Wang, H. M. Price, B. Zhang, and Y. D. Chong, Circuit implementation of a four-dimensional topological insulator, Nat. Commun. **11**, 2356 (2020).

[13] K. Yatsugi, S. E. Pandarakone, and H. Iizuka, Higher-order topological corner state in a reconfigurable breathing kagome lattice consisting of magnetically coupled LC resonators, Sci. Rep. **13**, 8301 (2023).

[14] A. Phutela, P. Bhumla, M. Jain, and S. Bhattacharya, Exploring strong and weak topological states on isostructural substitutions in $TlBiSe_2$, Sci. Rep. **12**, 21970 (2022).

[15] L. Fu, Topological crystalline insulators, Phys. Rev. Lett. **106**, 106802 (2011).

[16] F. Schindler, A. M. Cook, M. G. Vergniory, Z. Wang, S. S. P. Parkin, B. A. Bernevig, and T. Neupert, Higher-order topological insulators, Sci. Adv. **4**, eaat0346 (2018).

[17] A. Mook, S. A. Diaz, J. Klinovaja, and D. Loss, Chiral hinge magnons in second-order topological magnon insulators, Phys. Rev. B **104**, 024406 (2021).

[18] D. Zhu, M. Kheirkhah, and Z. Yan, Sublattice-enriched tunability of bound states in second-order topological insulators and superconductors, Phys. Rev. B **107**, 085407 (2023).

[19] N. Mao, R. Li, Y. Dai, B. Huang, B. Yan, and C. Niu, Orbital shift-induced boundary obstructed topological materials with a large energy gap, Adv. Sci. **9**, 2202564 (2022).

[20] C. Zhang, Y. Zhang, X. Yuan, S. Lu, J. Zhang, A. Narayan, Y. Liu, H. Zhang, Z. Ni, R. Liu *et al.*, Quantum Hall effect based on Weyl orbits in CD_3As_2, Nature (London) **565**, 331 (2019).

[21] F. Tang, Y. Ren, P. Wang, R. Zhong, J. Schneeloch, S. A. Yang, K. Yang, P. A. Lee, G. Gu, Z. Qiao *et al.*, Three-dimensional quantum Hall effect and metal-insulator transition in $ZrTe_5$, Nature (London) **569**, 537 (2019).

[22] R. Chen, T. Liu, C. M. Wang, H.-Z. Lu, and X. C. Xie, Field-tunable one-sided higher-order topological hinge states in Dirac semimetals, Phys. Rev. Lett. **127**, 066801 (2021).

[23] B. Fu, Z.-A. Hu, and S.-Q. ShenBulk-hinge correspondence and three-dimensional quantum anomalous Hall effect in second-order topological insulators, Phys. Rev. Res. **3**, 033177 (2021).

[24] S. Li, C. M. Wang, Z. Z. Du, F. Qin, H.-Z. Lu, and X. C. Xie, 3D quantum Hall effects and nonlinear Hall effect, npj Quantum Mater. **6**, 96 (2021).

[25] E. Khalaf, W. A. Benalcazar, T. L. Hughes, and R. Queiroz, Boundary-obstructed topological phases, Phys. Rev. Res. **3**, 013239 (2021).

[26] Y.-R. Ding, D.-H. Xu, C.-Z. Chen, and X. C. Xie, Hinged quantum spin Hall effect in antiferromagnetic topological insulators, Phys. Rev. B **101**, 041404(R) (2020).

[27] B. Lapierre, T. Neupert, and L. Trifunovic, Topologically localized insulators, Phys. Rev. Lett. **129**, 256401 (2022).

[28] F. D. M. Haldane, Model for a quantum Hall effect without Landau levels: Condensed-matter realization of the parity anomaly, Phys. Rev. Lett. **61**, 2015 (1988).

[29] J. M. Hou, Hidden-symmetry-protected topological semimetals on a square lattice, Phys. Rev. Lett. **111**, 130403 (2013).

[30] B. Ostahie, M. Nita, and A. Aldea, Edge-state mechanism for the anomalous quantum Hall effect in a diatomic square lattice, Phys. Rev. B **98**, 125403 (2018).

[31] J. M. Hou and W. Chen, Hidden antiunitary symmetry behind "accidental" degeneracy and its protection of degeneracy, Front. Phys. **13**, 130301 (2018).

[32] N. Biggs, *Algebraic Graph Theory*, 2nd ed. (Cambridge University Press, Cambridge, 1993).

[33] B. A. Levitan and T. Pereg-Barnea, Second-order topological insulator under strong magnetic field: Landau levels, Zeeman effect, and magnetotransport, Phys. Rev. Res. **2**, 033327 (2020).

[34] B. Ostahie, M. Nita, and A. Aldea, Electrical manipulation of edge states in graphene and the effect on quantum Hall transport, Phys. Rev. B **91**, 155409 (2015).

[35] R.-X. Zhang, F. Wu, and S. Das Sarma, Mobius insulator and higher-order topology in $MnBi_{2n}Te_{3n+1}$, Phys. Rev. Lett. **124**, 136407 (2020).

[36] C. Yue, Y. Xu, Z. Song, H. Weng, Y.-M. Lu, C. Fang, and X. Dai, Symmetry-enforced chiral hinge states and surface quantum anomalous Hall effect in the magnetic axion insulator $Bi_{2-x}Sm_xSe_3$, Nat. Phys. **15**, 577 (2019).

[37] G G. Liu, Z. Gao, Q. Wang, X. Xi, Y.-H. Hu, M. Wang, C. Liu, X. Lin, L. Deng, S. A. Yang *et al.*, Topological Chern vectors in three-dimensional photonic crystals, Nature (London) **609**, 925 (2022).

[38] C. H. Lee, S. Imhof, C. Berger, F. Bayer, J. Brehm, L. W. Molenkamp, T. Kiessling, and R. Thomale, Topolectrical circuits, Commun. Phys. **1**, 39 (2018).

[39] Z. Wang, Y. Biao, X.-T. Zeng, X. Chen, X.-L. Sheng, S. A. Yang, and R. Yu, Realization in circuits of a Chern state with an arbitrary Chern number, Phys. Rev. B **107**, L201101 (2023).

[40] C.-Z. Chang, J. Zhang, X. Feng, J. Shen, Z. Zhang, M. Guo, K. Li, Y. Ou, P. Wei, L.-L. Wang *et al.*, Experimental observation of the quantum anomalous Hall effect in a magnetic topological insulator, Science **340**, 167 (2013).

[41] T. Li, S. Jiang, B. Shen, Y. Zhang, L. Li, Z. Tao, T. Devakul, K. Watanabe, T. Taniguchi, L. Fu *et al.*, Quantum anomalous Hall effect from intertwined moiré bands, Nature (London) **600**, 641 (2021).

[42] B. A. Bernevig and T. L. Hughes, *Topological Insulators and Topological Superconductors* (Princeton University Press, Princeton, 2013).